




# Co<sub>3</sub>O<sub>4</sub>/NiO nanocomposite as a thermocatalytic and photocatalytic material for the degradation of malachite green dye

Waseeq Ur Rehman<sup>1,2</sup>, Muhammad Tayyab Noor Khattak<sup>1</sup>, Abdu Saeed<sup>3,4,\*</sup>, Kausar Shaheen<sup>5,6</sup>, Zarbad Shah<sup>2</sup>, Shah Hussain<sup>1</sup>, Esraa M. Bakhsh<sup>7</sup>, Haneen M. Alraddadi<sup>7</sup>, Taghreed M. Fagieh<sup>7</sup>, Kalsoom Akhtar<sup>7</sup>, Sher Bahadar Khan<sup>7,8</sup>, and Shahid Ali Khan<sup>9,\*</sup> 

<sup>1</sup>Department of Chemistry, Govt. Post Graduate College Nowshera, Nowshera 24100, Khyber Pakhtunkhwa, Pakistan

<sup>2</sup>Department of Chemistry, Bacha Khan University, Charsadda 24420, Khyber Pakhtunkhwa, Pakistan

<sup>3</sup>Department of Physics, Faculty of Science, King Abdulaziz University, Jeddah 21589, Saudi Arabia

<sup>4</sup>Department of Physics, Thamar University, 87246 Thamar, Yemen

<sup>5</sup>Department of Physics, Jinnah College for Women, University of Peshawar, Peshawar 25120, Khyber Pakhtunkhwa, Pakistan

<sup>6</sup>The Key Laboratory of Advanced Functional Materials, Ministry of Education, Beijing University of Technology, Beijing 100124, China

<sup>7</sup>Department of Chemistry, Faculty of Science, King Abdulaziz University, P.O. Box 80203, Jeddah 21589, Saudi Arabia

<sup>8</sup>Center of Excellence for Advanced Materials Research, King Abdulaziz University, P.O. Box 80203, Jeddah 21589, Saudi Arabia

<sup>9</sup>Department of Chemistry, School of Natural Sciences (SNS), National University of Sciences & Technology (NUST), H-12, Islamabad 44000, Pakistan

Received: 17 June 2022

Accepted: 30 October 2022

Published online:

7 January 2023

© The Author(s), under exclusive licence to Springer Science+Business Media, LLC, part of Springer Nature 2023

## ABSTRACT

Herein, the Co<sub>3</sub>O<sub>4</sub>/NiO nanocomposite has been synthesized as a catalyst for thermal degradation and photodegradation of the malachite green dye. Its morphology showed small spherical particles with an average particle size of  $52.82 \pm 17.73$  nm. The XRD pattern and XPS analysis proved the formation of Co<sub>3</sub>O<sub>4</sub>/NiO nanocomposite with the growth of both Co<sub>3</sub>O<sub>4</sub> and NiO at crystal contents proportions of  $67.7 \pm 17\%$  and  $32.3 \pm 16\%$ , respectively. The TGA results indicated that the Co<sub>3</sub>O<sub>4</sub>/NiO nanocomposite is nearly thermally stable up to 1000 °C. The synthesized Co<sub>3</sub>O<sub>4</sub>/NiO nanocomposite recorded an optical energy band gap of 4.27 eV and a surface area of 27.4933 m<sup>2</sup>/g. Besides, its photocatalytic activity was compared with the photolysis and thermocatalytic activity. The velocity constant ( $k_{app}$ ) value for photocatalysis was higher than that for photolysis by ten folds. Besides, various effects like dye concentration, pH, catalyst amount, and different scavengers were also evaluated.

Address correspondence to E-mail: Abdusaeed@tu.edu.ye; shahid.ali@sns.nust.edu.pk

<https://doi.org/10.1007/s10854-022-09428-7>

## 1 Introduction

Environmental pollution has become paramount attention in recent years [1], posing a threat to human life and causing ecological imbalance [2]. Pollution can come from industry effluents such as dyes [3]. In the garment, dyes are commonly used; most of our daily life products, such as clothes, drinks, food materials, homes, and even medication, are colored by dyes. They are categorized according to their composition, coloring properties, and solubility, and there are approximately 10,000 commercially synthetic dyes in the market [4]. Congo red, methylene blue, rhodamine-B, methyl orange, and other dyes are used as a colorant in processing on a wide scale. However, they are released into the water, posing severe health risks [5]. They can threaten our health and destroy the environment [6]; they are considered major pollutants in water [7, 8], making a foam-like layer on the water's surface and preventing the passage of light and air, affecting aquatic life flora, and fauna. Therefore, wastewater treatments are imperative every day and necessary for human life.

Traditional biological treatment techniques are inadequate for removing chemical pollutants. Therefore, eco-friendly techniques become at this time urgently to clean and or remove harmful chemicals [9]. Therefore, green chemistry applies chemical methods, pathways, and methodologies that reduce or exclude the use or production of harmful feedstock, materials, byproducts, reagents, and solvents, among other things. Consequently, the primary goal of green chemistry is to reduce toxic chemical systems and materials, which are critical to the global economy, while still maintaining the high quality of life that we enjoy [10]. Many techniques are used to eliminate organic dyes, such as adsorption [11–13], electrocoagulation [14], Fenton-oxidation [15], advanced oxidation processes [16], electrochemical advanced oxidation processes [17], and membrane technology [18, 19]. Among these different technologies, the advanced oxidation process is one of the most demanding and emerging techniques that use nanocatalysis to convert toxic contaminants to non-toxic inorganic compounds such as  $\text{CO}_2$  and  $\text{H}_2\text{O}$  in the presence of light [5].

Malachite green (MG) is a well-known organic dye containing the triphenylmethane group; it is used in coloring in industries. Due to its toxic effects, MG dye

has attracted much attention from synthetic dye contaminants [20]. Its color has a detrimental influence on the reproductive and immune systems [21]. Moreover, MG dye has been used extensively by the agriculture industry and is widely used as a coloring agent in different industries. However, besides its extensive use in various industries, this dye is a controversial molecule as it is reported in fish or other aquatic animals, so it poses a high risk to the consumer, who uses foodstuff. MG dye is reported to have mutagenic and carcinogenic effects as well as an adverse effect on the reproductive system [22]. Photocatalysis, biological treatment, ultrafiltration, advanced oxidation processes, and the adsorption process have all been used to remove the MG dye [23–25]. However, there is still a lack of proper catalysts that perfectly remove the wastewater's MG dye. Different nanocomposites, either in the form of powders or thin films [26–31], have been innovated to be used as photocatalysts. In this work,  $\text{Co}_3\text{O}_4/\text{NiO}$  nanocomposite was synthesized via the sol-gel method. Then, the synthesized nanocomposite was used as a catalyst for the remediation and degradation of MG dye through thermocatalysis and photocatalysis. As far as we know, this is the first time that the  $\text{Co}_3\text{O}_4/\text{NiO}$  nanocomposite has been used to degrade MG.

## 2 Experimental

### 2.1 Chemicals and reagents

Cobalt(II) chloride hexahydrate ( $\text{CoCl}_2 \cdot 6\text{H}_2\text{O}$ ), nickel(II) chloride hexahydrate ( $\text{NiCl}_2 \cdot 6\text{H}_2\text{O}$ ), and sodium hydroxide (NaOH) were acquired from Sigma-Aldrich (Sigma-Aldrich, Germany). MG dye was acquired from BDH chemicals ltd (BDH, UK). All the chemicals were used as they were without any further purification.

### 2.2 Synthesis of $\text{Co}_3\text{O}_4/\text{NiO}$ nanocomposite

$\text{Co}_3\text{O}_4/\text{NiO}$  nanocomposite was synthesized via the sol-gel method [32–34]. Briefly,  $\text{NiCl}_2 \cdot 6\text{H}_2\text{O}$  and  $\text{CoCl}_2 \cdot 6\text{H}_2\text{O}$  salts were thoroughly mixed in a stoichiometric amount and dissolved in distilled water in a  $1 \text{ dm}^3$  Erlenmeyer flask and agitated for 30 min without heating at room temperature (RT). Then, in a

drop-by-drop process, one molar of sodium hydroxide solution was added to the blender until pH 10 was achieved. Then blender was warmed up to 70 °C for 7 h with continuous mixing on a magnetic stirrer hot plate. After that, the precipitate was washed several times with an ethanol–water mixture (1:4). The resultant paste was desiccated in an oven for 8 h at 50 °C. The dried cake was powdered and put in a furnace at 400 °C for six hours for activation. A simple presentation for the preparation of  $\text{Co}_3\text{O}_4/\text{NiO}$  nanocomposite is given in Scheme 1.

### 2.3 Characterization techniques

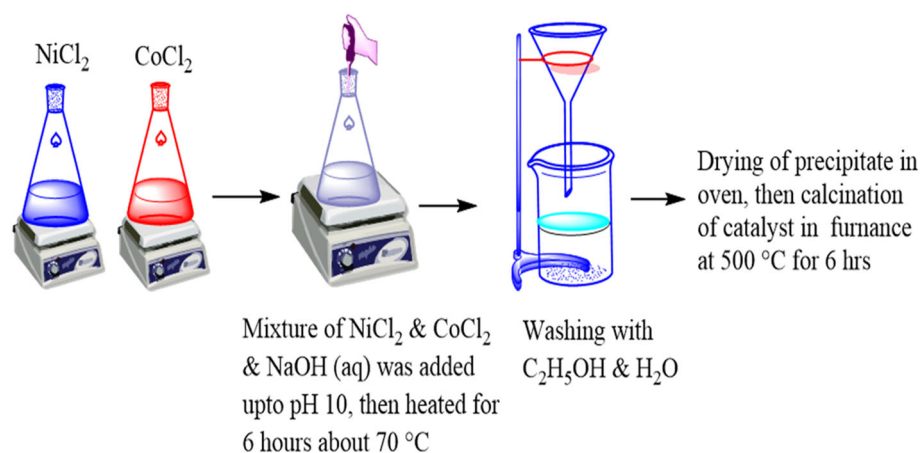
The synthesized  $\text{Co}_3\text{O}_4/\text{NiO}$  nanocomposite was characterized and studied by different spectroscopic and analytical techniques. The surface morphology and textural characteristics of  $\text{Co}_3\text{O}_4/\text{NiO}$  nanocomposite were studied on field-emission scanning electron microscopy (FESEM) model FEI Quanta 450 (FEI, USA). The elemental analysis and oxidation state of the  $\text{Co}_3\text{O}_4/\text{NiO}$  nanocomposite were determined on the X-ray photoelectron spectroscopy (XPS) model ESCALAB-250Xi (Thermo Scientific, UK). X-ray diffraction (XRD) was used to investigate the crystal structure and crystal phase of the synthesized  $\text{Co}_3\text{O}_4/\text{NiO}$  nanocomposite powder using an XRD machine model D8 ADVANCE (Bruker, USA) having a  $\text{CuK}\alpha$  radiation wavelength source. Similarly, the thermal stability of the nanocatalyst was investigated through the thermogravimetric analyzer (TGA) model Pyris 1-TG (Perkin-Elmer, USA), and optical characteristics were achieved through UV–Vis spectrophotometer model UV 2800 (Wincom, China). The average pore volume, aperture size, and surface area were determined through  $\text{N}_2$  adsorption/desorption

experiments, recorded on BET model JW-BK300 (JWGB, China). The proceeding of the MG dye degradation was inspected through ultraviolet/visible (UV–Vis) spectrophotometer model Evolution™ 350 UV–Vis (Thermo Scientific, USA).

### 2.4 Degradation of MG

The degradation investigation was executed in 50 mL of the beaker containing 30 mL of 0.05 mM MG dye mixture and 0.05 g of  $\text{Co}_3\text{O}_4/\text{NiO}$  nanocomposite. Firstly, we tested the effect of contact time, where 0.05 mM of 50 mL of MG dye was taken in a conical flask with 0.05 g of  $\text{Co}_3\text{O}_4/\text{NiO}$  nanocomposite at 313 K. Then, 5 mL of dye was sampled every 10 min, and the reaction proceeding was recorded on the UV–Vis spectrophotometer. It was detected that the rate of MG dye degradation was initially higher and decreased as the reaction progressed. The experiments were set to proceed for 120 min. Various concentrations of MG dye, i.e., 0.01 mM, 0.02 mM, 0.03 mM, and 0.04 mM, were investigated to examine the influence of the concentration under similar experimental conditions. The thermocatalysis of the MG dye solution was investigated at the temperature range of 278–313 K. Furthermore, the pH effect was tested in the presence of solar light. Similarly, the catalyst dosages were investigated using 0.01 g, 0.03 g, 0.05 g, 0.09 g, 0.1 g, and 0.5 g  $\text{Co}_3\text{O}_4/\text{NiO}$  nanocomposite. The free radical scavenger assay was performed using 0.05 mM of MG dye solution with 0.5 g of the  $\text{Co}_3\text{O}_4/\text{NiO}$  nanocomposite under the influence of solar light. All the experiments were carried out under visible light or solar light with continuous mixing. The degradation of MG was followed by decolorization that was performed through

**Scheme 1** General Scheme for the formulation of  $\text{Co}_3\text{O}_4/\text{NiO}$  nanocomposite



UV–Vis spectrophotometer. The following equation was used to compute the percent degradation of MG.

$$\text{R.E. \%} = \frac{A_0 - A_t}{A_0} \quad (1)$$

R.E. % stands for the percent removal efficiency. It stands for absorption assessment at time  $t$  (min), and  $A_0$  is the absorption assessment of the first original blend.

Likewise, the velocity constant ( $k_{\text{app}}$ ) values were acquired from the pseudo-1st-order kinetic study as displayed by the following equation:

$$\ln \frac{C_t}{C_0} = k_{\text{app}} t + C \quad (2)$$

$$t_{1/2} = \frac{0.693}{k} \quad (3)$$

where  $C_0$  and  $C_t$  are the concentrations of the MG mixture at the start point and time  $t$ , respectively. Equation 3 indicates the half-life of pseudo first-order kinetics, where  $k$  indicates the rate constant value.

## 3 Results and discussion

### 3.1 Characterizations

#### 3.1.1 FESEM

Figure 1a shows the image of FESEM at low resolution, representing the  $\text{Co}_3\text{O}_4/\text{NiO}$  nanocomposite framework. This image indicated that the  $\text{Co}_3\text{O}_4/\text{NiO}$  nanocomposite has nearly spherical shapes. Also, a mixture of individual particles and clusters can be seen in the low-resolution FESEM image; therefore, the FESEM image with high resolution was captured for the cluster and is shown in Fig. 1b. The high-resolution FESEM revealed that these clusters are aggregated small spherical particles. The aggregations of small particles create irregular larger particles with more pores (Fig. 1b). We estimated the synthesized  $\text{Co}_3\text{O}_4/\text{NiO}$  nanocomposite particle sizes; their distribution histograms are shown in Fig. 1c. The mean particle size was  $52.82 \pm 17.73$  nm.

#### 3.1.2 XPS

The chemistry and the elemental composition of  $\text{Co}_3\text{O}_4/\text{NiO}$  nanocomposite were studied by using XPS. Figure 2a indicates the existence of C, Cl, Co,

Na, Ni, and O elements with their binding energies. The elements of Cl and Na are residues of the reactant we used to synthesize the composite, while the presence of C is due to the carbon tape that we utilized as a substrate to perform the XPS examination. The XPS, Co 2p, Ni 2P, and O 1s peaks have been deconvoluted to understand more about the oxidation states. Figure 2b displays deconvoluted Co 2p that comprises two strong peaks,  $2p_{3/2}$  and  $2p_{1/2}$ , at 780.9 and 796.36 eV, with their satellite (sat) peaks at 785.46 and 803.08 eV, indicating the presence of  $\text{Co}^{+2}$  and  $\text{Co}^{+3}$  in  $\text{Co}_3\text{O}_4$  [34, 35]. Similarly, Fig. 2c displays the deconvoluted Ni 2p that shows two prominent peaks,  $2p_{3/2}$  and  $2p_{1/2}$ , at 855.74 and 873.69 eV, with their sat peaks at 861.71 and 880.05 eV; proving the existence of NiO in the  $\text{Co}_3\text{O}_4/\text{NiO}$  nanocomposite. The binding energy of the O 1s state displays a peak, which belongs to the multiple oxygen interactions with Ni and Co in  $\text{Co}_3\text{O}_4/\text{NiO}$  nanocomposite. Figure 4d shows the O 1s deconvoluted into two peaks centered at 535.1 and 531.15 eV; these two peaks could correspond to the binding energy of the oxygen of Ni and Co, respectively. It can be observed that the peak Co–O is higher than the peak of Ni–O, reflecting the ratios of  $\text{Co}_4\text{O}_3$  (67.7%) and NiO (32.3%) (see the XRD analysis results in Table 1).

#### 3.1.3 XRD

The XRD models are usually utilized to analyze the crystallinity of the materials, identify their crystal phases, and estimate the crystallite sizes. XRD patterns of the prepared nickel oxide and cobalt oxide nanocomposite ( $\text{Co}_3\text{O}_4/\text{NiO}$ ) are shown in Fig. 3a. The sample's XRD pattern showed different peaks, which indicates a crystalline structure in the synthesized sample. Cards of the International Centre for Diffraction Data (ICDD) were used to characterize the RPD pattern, where the XRD pattern's diffracted peaks coincided with the tricobalt tetraoxide ( $\text{Co}_3\text{O}_4$ ) ICDD (PDF-2/Release 2011 RDB) card no. 01-074-1656 and nickel oxide (NiO) ICDD (PDF-2/Release 2011 RDB) card no. 01-078-4370. According to the ICDD card no. 01-074-1656, the peaks at positions of  $31.68^\circ$ ,  $44.46^\circ$ ,  $55.53^\circ$ ,  $59.16^\circ$ ,  $65.27^\circ$ ,  $73.80^\circ$ , and  $76.96^\circ$  are associated with atoms planes that, respectively, have the Miller indices of (220), (400), (331), (422), (511), (440), (620), and (533) of the  $\text{Co}_3\text{O}_4$  crystal structure. While according to the ICDD card no. 01-078-4370, the peaks at  $2\theta$  numerical values of  $36.82^\circ$ ,

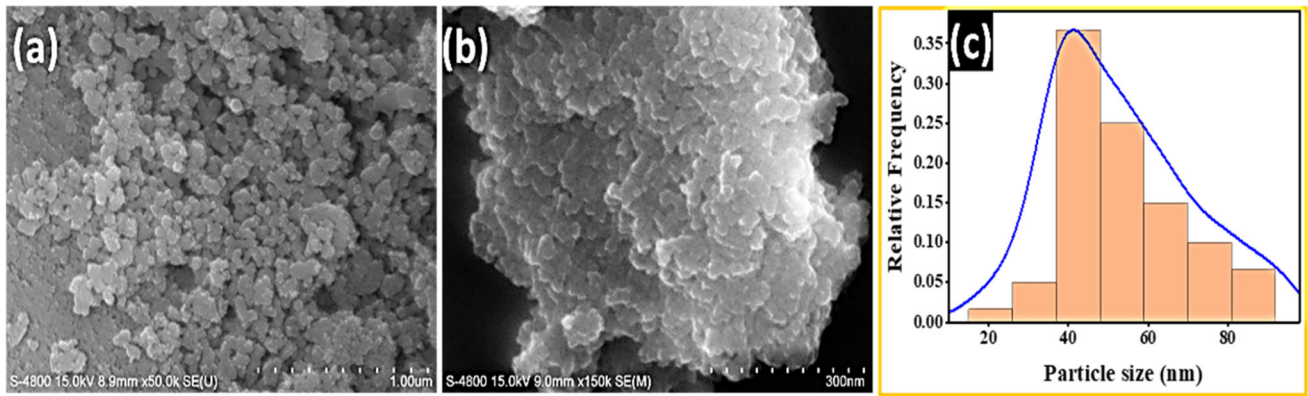


**Fig. 1** FESEM results of  $\text{Co}_3\text{O}_4/\text{NiO}$  nanocomposite **a** low resolution **b** high resolution **c** particle size distribution histogram

**Fig. 2** XPS spectra of  $\text{Co}_3\text{O}_4/\text{NiO}$  nanocomposite **a** full range of XPS spectrum **b** Ni 2p **c** Co 2p **d** O 1s

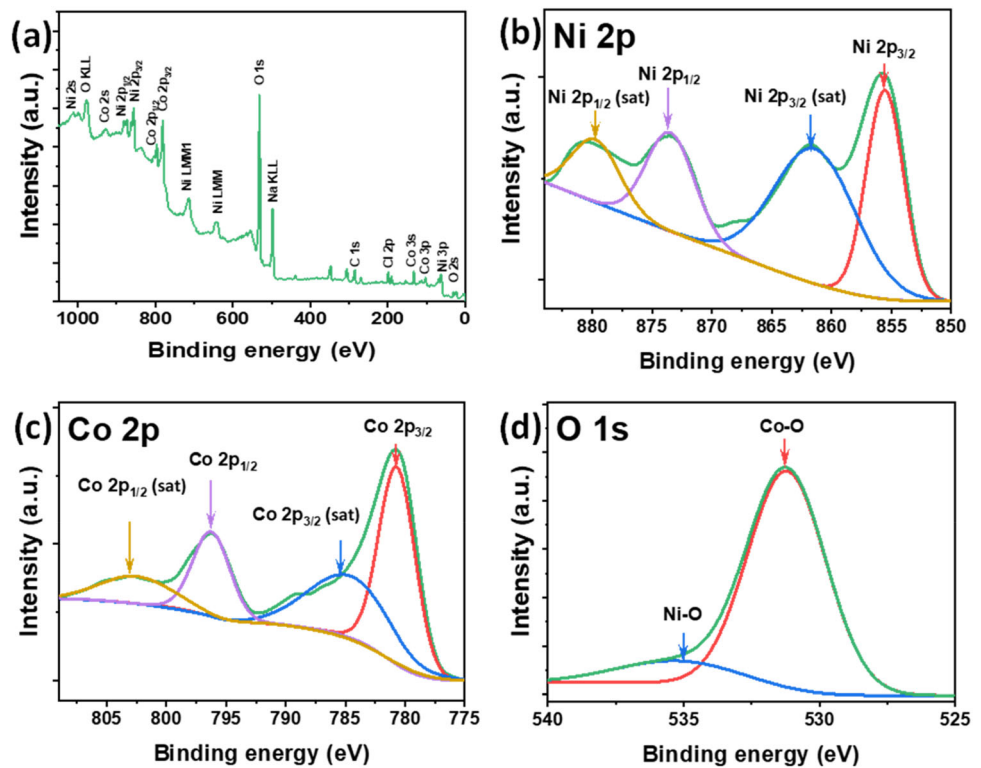


**Table 1** The crystal phase of the synthesized  $\text{Co}_3\text{O}_4/\text{NiO}$  nanocomposite sample with its lattice parameters and ratios achieved from the XRD study

Crystal phase	Chemical formula	Lattice parameters (Å)			Crystallite size (nm)	Ratio (%)
		<i>a</i>	<i>b</i>	<i>c</i>		
Cobalt oxide	$\text{Co}_3\text{O}_4$	8.1004	8.1004	8.1004	$7.50 \pm 9$	$67.7 \pm 17$
Nickel oxide	NiO	2.9714	2.9714	7.2876	$7.96 \pm 3$	$32.3 \pm 16$

43.26°, 62.85°, 75.29°, and 78.69° are associated with the atoms planes that have the Miller indices of (101), (012), (104), (021), and (006), respectively, of the NiO crystal structure. The structural refinement was carried out in the XRD pattern using the Rietveld

analysis. The B-spline function was applied to model the shapes of the diffraction peaks. The matching to the pdf cards manifested that the cobalt oxide phase is a cubic crystal system that has framework parameters  $a = b = c = 8.1004 \text{ \AA}$  with  $\text{Fd}\bar{3}\text{m}$  space group. In

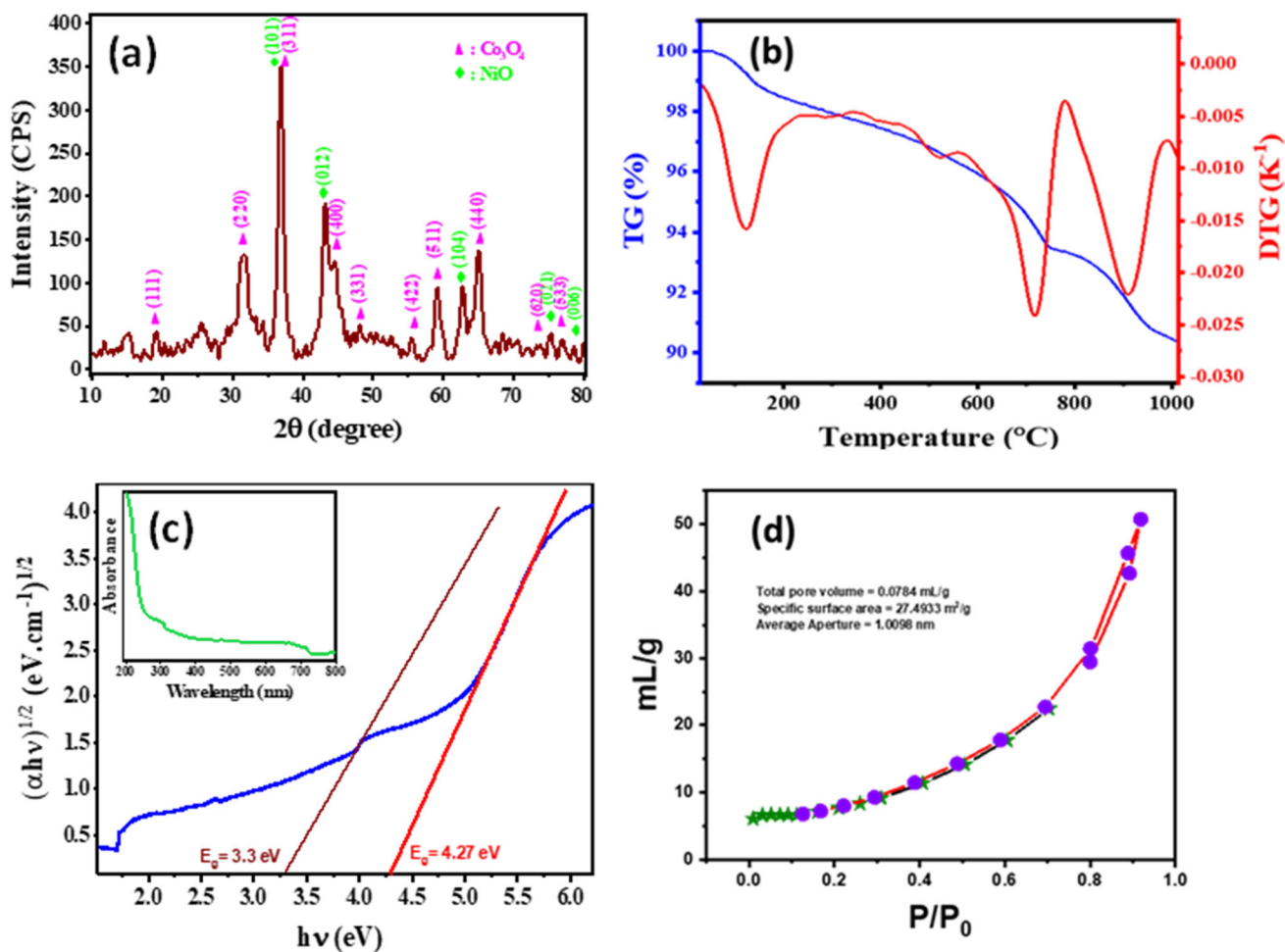


**Fig. 3** Characterizations of synthesized  $\text{Co}_3\text{O}_4/\text{NiO}$  nanocomposite **a** XRD patterns **b** TG curve and its DTG curve **c** the optical band gap energy of  $\text{Co}_3\text{O}_4/\text{NiO}$  nanocomposite, the inset shows the UV-vis absorption spectrum **d** BET analysis of  $\text{Co}_3\text{O}_4/\text{NiO}$  nanocomposite

contrast, the nickel oxide phase is a trigonal crystal system that has lattice parameters  $a = b = 2.98261 \text{ \AA}$  and  $c = 7.28763 \text{ \AA}$  with  $R\bar{3}m$  space group. The XRD results, i.e., the presence of NiO and  $\text{Co}_3\text{O}_4$  phases, agree with the XPS results. The crystal phase content of cobalt oxide and nickel oxide was estimated using reference intensity ratio (RIR), where they recorded  $67.7 \pm 17\%$  and  $32.3 \pm 16\%$ , respectively. Based on whole powder pattern fitting (WPPF), the average crystallite sizes of their phases were evaluated via Scherrer's equation (Eq. 3) based on full width at half maximum calculated by whole powder pattern fitting (WPPF) [36].

$$D = \frac{0.94\lambda}{\beta \cos \theta} \quad (4)$$

where  $D$  is the grain size of the crystal phase;  $\beta$  is the full width at half maximum (FWHM) of the

diffraction peak,  $\theta$  is the angle of diffraction, and  $\lambda$  is the wavelength used in XRD ( $\lambda = 1.54 \text{ \AA}$ ). The crystallite sizes were found to be  $7.50 \pm 3 \text{ nm}$  and  $7.93 \pm 9 \text{ nm}$  for cobalt and nickel oxides, respectively. Table 1 summarizes all achievement XRD results. The details of the performed XRD analysis were included in a separate file (Electronic Supplementary Materials).

### 3.1.4 TGA

The decomposition conduct of the synthesized  $\text{Co}_3\text{O}_4/\text{NiO}$  nanocomposite was investigated using TGA; Fig. 3b displays the TGA curve and its first derivative (DTG) in the temperature range 30–1000 °C. A total of 9.61% weight loss till 100 °C indicating the thermal stability of the synthesized catalyst. The TGA curve shows that the weight

loss occurred in three steps and manifested as peaks in the DTG plot. The weight loss (1.29%) in the first step in the TGA curve in the range of 70–150 °C is due to the evaporation of the leftover water in the synthesized composite. The second step's weight loss (5.31%) started from 120 to 750 °C; this step has slow decomposition, possibly due to the conversion of residual precursor nickel chloride to nickel oxide [37]. The weight loss (3.01%) in the third step happened after 750 °C up to 1000 °C in the TGA curve; this step could occur due to inspiring defects in the Co<sub>3</sub>O<sub>4</sub>/NiO nanocomposite, which could be associated with the oxygen loss, consolidating the oxygen vacancies formation [38]. The DTG curve manifested three prominent peaks corresponding to the TGA curve's three steps. The first peak, centered at 114 °C, corresponds to the first step in the TGA step, which was referred to as the water's evaporation. The second peak in the DTG centered at 712 °C, which corresponds to the second peak in the TGA curve, this peak could result from the oxidation of nickel chloride into nickel oxide [37]. The DTG third peak centered at 910 °C could be assigned to the oxygen vacancies formation in the prepared Co<sub>3</sub>O<sub>4</sub>/NiO nanocomposite [38].

### 3.1.5 UV-Vis

The UV-Vis spectrum of Co<sub>3</sub>O<sub>4</sub>/NiO nanocomposite was performed in the range of 200–800 nm; the recorded UV-Vis spectrum is exhibited in inset Fig. 3c. An absorption edge was noticed in the UV-Vis spectral range of 200–250 nm. The Co<sub>3</sub>O<sub>4</sub>/NiO nanocomposite's optical bandwidth ( $E_g$ ) was esteemed using the Tauc relation given by the following equation:

$$(\alpha h\nu)^{1/n} = A(h\nu - E_g) \quad (5)$$

where  $\alpha$  is the absorption coefficient,  $h$  is the Planck constant,  $\nu$  is the photon frequency, and  $A$  is a constant. Here,  $n$  is an exponent, which depends on the material's quantum selection rules;  $n = 1/2$  designed for allowed direct electronic transition;  $n = 3/2$  intended for direct forbidden transition; and  $n = 2$  for indirect allowed electronic transition. The Co<sub>3</sub>O<sub>4</sub>/NiO nanocomposite was reported as an optical indirect energy band gap,  $E_g$  [39]. Figure 3c displays the Tauc plot of the Co<sub>3</sub>O<sub>4</sub>/NiO nanocomposite. The magnitude of  $E_g$  was estimated via extrapolation of linear regions of the plot of  $(\alpha h\nu)^{1/2}$  against  $h\nu$ . The

curve of  $(\alpha h\nu)^{1/2}$  revealed two linear regions with the two intercepts at 4.27 and 3.3 eV, suggesting two energies band gap that could be attributed to the two phases included in the nanocomposites, i.e., Co<sub>3</sub>O<sub>4</sub> and NiO. The long linear portion of the curve of  $(\alpha h\nu)^{1/2}$  (line presented in red color) showed an intercept at 4.27 eV; this value could represent the energy band gap of the NiO phase because several studies [40–43] reported its energy band gap in the range of 3.6–4.47 eV, while the short portion of the curve of  $(\alpha h\nu)^{1/2}$  (line presented in wine color) showed intercept at 3.3 eV could belong to the Co<sub>3</sub>O<sub>4</sub> phase because its energy band gap reported in several studies [44–46] as in the range of 1.29–3.65 eV, where the variations in the band gap values were referred to the quantum confinement effect resulting and grain size [44–46]. In final words, these results suggest that the 4.27 and 3.3 eV represent the values of the energy band gap of the NiO and Co<sub>3</sub>O<sub>4</sub>, respectively.

### 3.1.6 BET

The N<sub>2</sub> adsorption-desorption experiment was performed at 77 K in an inert atmosphere of He gas. The Brunauer-Emmett-Teller (BET) experiments revealed a 27.4933 m<sup>2</sup>/g surface area and an average aperture size of 1.0098 nm. The total pore volume is 0.0784 mL/g, as shown in Fig. 3d. The excellent surface capacity and high aperture volume suggest the homogenous particle size of the Co<sub>3</sub>O<sub>4</sub>/NiO nanocomposite.

## 3.2 Catalyst activity

### 3.2.1 Thermocatalysis

Figure 4a shows the results of the thermocatalysis experiments achieved from 30 mL of 0.05 mM MG dye and 0.05 g of Co<sub>3</sub>O<sub>4</sub>/NiO nanocomposite at temperatures of 278 K, 293 K, 303 K, and 313 K proceed for 120 min. As evident from this figure, the highest percent degradation of MG was achieved at 313 K, which was 95.3% (Table 2) at 120 min, followed by 93.7% at 303 K, and the lowest at 278 K, which was 82.6%. The thermocatalysis experiments indicated that the rate of MG dye degradation upsurges with an upsurge in temperature. Thus, the highest velocity constant value was obtained at 313 K ( $2.37 \times 10^{-2} \text{ min}^{-1}$ ), while the lowest  $k_{\text{app}}$  value was

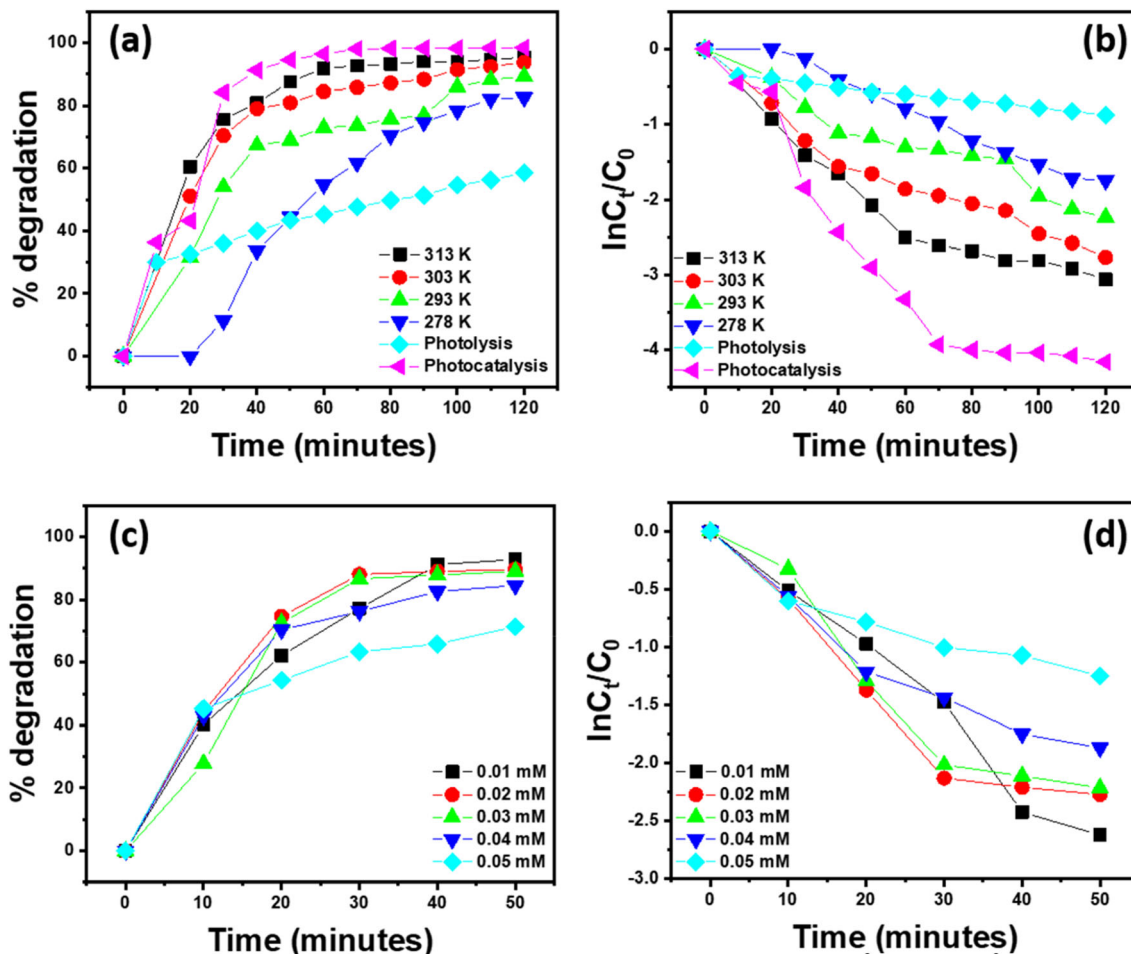


**Fig. 4** Catalyst activity of synthesized  $\text{Co}_3\text{O}_4/\text{NiO}$  nanocomposite on the degradation of MG dye **a** percent degradation value of MG dye obtained from thermocatalysis, photolysis, and photocatalysis experiment **b**  $\ln(C/C_0)$ -time relationship obtained from various

thermocatalysis, photolysis and photocatalysis **c** percent degradation value of MG dye obtained from the initial concentration of MG dye **d**  $\ln(C/C_0)$ -time relationship obtained at different concentrations

obtained at 278 K ( $1.72 \times 10^{-2} \text{ min}^{-1}$ ). It seems that the photocatalyst is temperature dependent, and an increase in temperature will increase the rate of MG degradation. The increase in temperature will possibly decrease the activation energy for the MG

degradation as well as decrease the HOMO-LUMO band gap of the catalyst. The  $k_{app}$ ,  $R^2$ , and percent degradation of MG dye are summarized in Table 2.

**Table 2** Temperature,  $k_{app}$ , percent degradation, and  $R^2$  numerical values of MG degradation by using thermocatalysis, photocatalysis, and photolysis and thermolysis experiments

Parameters	Temperature (K)	$k_{app}$ ( $\text{min}^{-1}$ )	$R^2$	$t_{1/2}$ ( $\text{min}^{-1}$ )	Percent degradation
thermocatalysis	313	$2.37 \times 10^{-2}$	0.8830	29.24	95.30
	303	$2.05 \times 10^{-2}$	0.9343	33.80	93.70
	293	$1.73 \times 10^{-2}$	0.9497	40.06	89.30
	278	$1.72 \times 10^{-2}$	0.9747	40.29	82.60
Photolysis	293	$3.95 \times 10^{-3}$	0.8934	175.44	57.60
Photocatalysis	293	$3.95 \times 10^{-2}$	0.8752	17.54	99.70
Thermolysis	293	$1.60 \times 10^{-3}$	0.9616	433.13	14.98
	303	$8.30 \times 10^{-3}$	0.9534	83.49	59.73
	313	$1.50 \times 10^{-2}$	0.8409	45.00	80.82



### 3.2.2 Photolysis

Figure 4a also displays the results of the photolysis experiment achieved under the solar light without catalyst under the same condition mentioned above for the thermocatalysis at temperature 293. This experiment investigated the role of solar light only on the down gradation of MG aqueous solution. As presented in Fig. 4a and Table 2, only 57.6% of the MG dye was degraded in 120 min. This result suggested that solar light has a role in the degradation of MG dye. The  $k_{app}$  value was  $3.95 \times 10^{-3} \text{ min}^{-1}$  (Table 2).

### 3.2.3 Photocatalysis

After completing thermocatalysis and photolysis experiments, the role of catalyst in the incidence of solar illumination was investigated in the down gradation of MG pigment. The catalyst has a predominant role in the degradation of MG dye in the company of  $\text{Co}_3\text{O}_4/\text{NiO}$  nanocomposite. As evident from Table 2 and Fig. 4a, the percent down gradation of MG dye was highest in the presence of solar light by using  $\text{Co}_3\text{O}_4/\text{NiO}$  nanocomposite. Approximately, 100% of the MG dye was degraded in 120 min with the  $k_{app}$  value of  $3.95 \times 10^{-2} \text{ min}^{-1}$ . Approximately, 98% of the MG dye was degraded in 60 min, and onward the degradation was negligibly changing till 120 min as the dye was almost completely degraded. The photocatalysis results suggested that the  $\text{Co}_3\text{O}_4/\text{NiO}$  nanocomposite has a chief character in the degradation of MG dye under solar light illumination. The solar light provided photons that can easily promote the electrons between valance and conduction band, facilitating the degradation of MG dye. 30 mL of 0.05 mM of MG dye solution was treated with 0.3 g of the  $\text{Co}_3\text{O}_4/\text{NiO}$  nanocomposite in a complete dark condition at room temperature to know the adsorption potential of the catalyst. It was observed that only 10% of the MG dye was adsorbed in 1 h on  $\text{Co}_3\text{O}_4/\text{NiO}$  catalyst.

### 3.2.4 Thermolysis

The thermolysis is done in the absence of catalyst and in a complete dark reaction. The sample is heated in water bath at 293, 303, and 313 K. The superior catalyst activity was displayed by photocatalysis at 293 K with a  $k_{app}$  value of  $3.95 \times 10^{-2} \text{ min}^{-1}$  and

lowest by thermolysis at 293 K with a  $k_{app}$  value of  $1.60 \times 10^{-3} \text{ min}^{-1}$ , respectively. The shortest half-life was calculated for photocatalysis which was  $17.54 \text{ min}^{-1}$ . We concluded this section that the highest degradation rate of MG dye was achieved with photocatalysis at room temperature.

### 3.2.5 Effect of concentration

Concentration optimization is a crucial step in the degradation of any pollutant. Figure 4c displays the MG degradation at different concentrations in the range of 0.01–0.05 mM. In this experiment, 0.05 g of  $\text{Co}_3\text{O}_4/\text{NiO}$  nanocomposite was used and illuminated in solar light for 70 min. As manifested in this figure and Table 3, the highest rate was observed when the concentration was low, but as we increased the concentration, the  $k_{app}$  decreased. For instance, the  $k_{app}$  value of 0.01 mM of the MG dye solution was higher ( $5.52 \times 10^{-2} \text{ min}^{-1}$ ); then, when the concentration of the MG in the solution was increased (0.05 mM), the  $k_{app}$  value decreased significantly ( $3.95 \times 10^{-3} \text{ min}^{-1}$ ). Approximately, 93.5% of MG dye was degraded during 70 min when the solution contained 0.01 mM of MG; however, at the same interval time, the solution's degradation of 0.05 mM of MG was 71.3. The decline in the catalyst activity at 0.05 mM is due to the high transport of MG molecules to the active sites of the catalyst, as compared to the less transport of MG molecules in the case of 0.01 mM MG molecules. Thus, access to the active sites by MG molecules at high concentrations is difficult; therefore, the reaction rate at high concentrations declined.

### 3.2.6 Effect of pH

Various pH values were studied to investigate the effect of pH on the activity of the synthesized  $\text{Co}_3\text{O}_4/\text{NiO}$  nanocomposite while degrading the MG dye in solar light for 120 min. The pH below 7 was made by drop-wise addition of dilute HCl, and the pH above 7 was attuned via the addition of a dilute solution of NaOH. As manifested in Fig. 5a, the degradation of MG dye is higher in the basic medium while lowest in the acidic medium. As the acidic medium increases, the degradation of MG dye decreases. For instance, the MG degradation was approximately 89% at pH 2, while it was 99% at pH 8. As the photocatalysis occurs on the catalyst surface, therefore,

**Table 3**  $k_{app}$ , percent degradation, and  $R^2$  values of varied concentrations of MG at room temperature

Concentration (mM)	$k_{app}$ ( $\text{min}^{-1}$ )	$R^2$	Percent degradation
0.01	$5.52 \times 10^{-2}$	0.9809	93.5
0.02	$2.05 \times 10^{-2}$	0.9343	91.7
0.03	$1.73 \times 10^{-2}$	0.9497	89.8
0.04	$1.72 \times 10^{-2}$	0.9747	84.5
0.05	$3.95 \times 10^{-3}$	0.8752	71.3

the surface charge changes greatly with a change in pH, and thus, the performance of the photocatalyst is greatly dependent on the pH variation. The degradation rate is higher at the high pH of the MG dye solution (alkaline pH) because the negative surface will attract the positive MG dye.

### 3.2.7 Effect of adsorbent dose

This test was carried out at various adsorbent amounts of 0.03 g, 0.05 g, 0.09 g, 0.1 g, 0.2 g, and 0.5 g. Figure 5b shows the achieved results of MG degradation by using different amounts of the synthesized  $\text{Co}_3\text{O}_4/\text{NiO}$ . The obtained results indicated that the degradation process was increased with an increasing amount of the adsorbent dose. The highest degradation was observed with 0.5 g of the  $\text{Co}_3\text{O}_4/\text{NiO}$  catalyst compared to the low adsorbent dose. The degradation percentage was 99% at 0.5 g of the catalyst, while it decreased to approximately 91% when the adsorbent dose was 0.01 g. The adsorbent dose has a specific limit, and after that limit, the degradation remains constant [47]. At high adsorbent doses, the surface-active sites may be blocked, and the access of light to the active sites may decrease; therefore, the rate of degradation decreases.

### 3.2.8 Effect of scavengers

Free radical scavenging assay is one of the most critical studies in photocatalysis because it provides a suggested mechanistic pathway for the degradation of pollutants. For this purpose, we selected sugar,  $\text{H}_2\text{O}_2$ , EDTA, and methanol ( $\text{CH}_3\text{OH}$ ), which are hydroxyl free radicals ( $\cdot\text{OH}$ ) and hole ( $\text{h}^+$ ) scavengers. As evident from Fig. 5c, EDTA,  $\text{H}_2\text{O}_2$ , and sugar predominantly suppress the catalyst activity, while  $\text{CH}_3\text{OH}$  negatively impacts the  $\text{Co}_3\text{O}_4/\text{NiO}$  catalyst activity. Therefore, we can predict that  $\cdot\text{OH}$  free radicals are concerned with the chemical degradation of MG dye. The probable mechanism for the results shown in Fig. 5c is illustrated in the next section.

## 3.3 Probable mechanism

Free radicals play a crucial role in the degradation of organic pollutants. For instance, EDTA is a hole scavenger, and  $\text{CH}_3\text{OH}$  is an  $\cdot\text{OH}$  free radical scavenger [48, 49]. The experiments revealed that adding methanol has a negligible effect on the degradation performance. In contrast, the  $\text{H}_2\text{O}_2$  and sugar showed a significant effect on the degradation of MG dye. The degradation performance of  $\text{Co}_3\text{O}_4/\text{NiO}$  was 74%

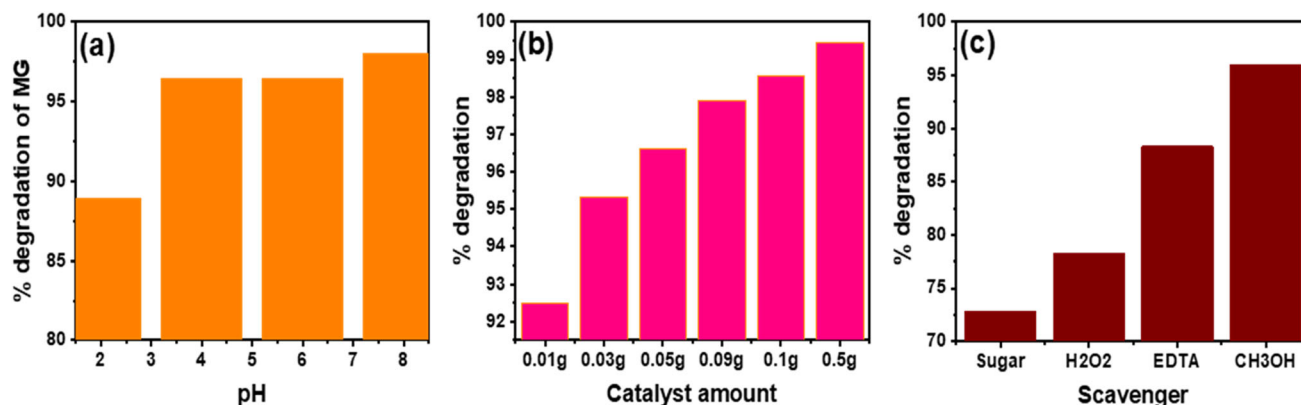


**Fig. 5** Catalyst activity of synthesized  $\text{Co}_3\text{O}_4/\text{NiO}$  nanocomposite on the degradation of MG dye under **a** influence of pH **b** influence of adsorbent dose **c** different selected scavengers

**Scheme 2** Probable mechanism of MG dye degradation by synthesized  $\text{Co}_3\text{O}_4/\text{NiO}$  nanocomposite

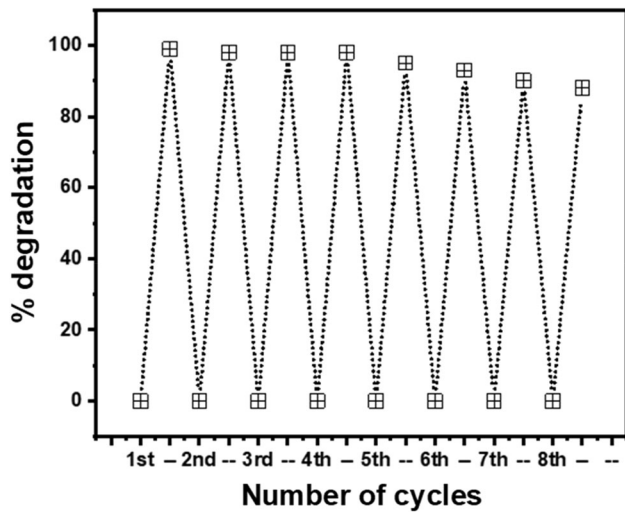
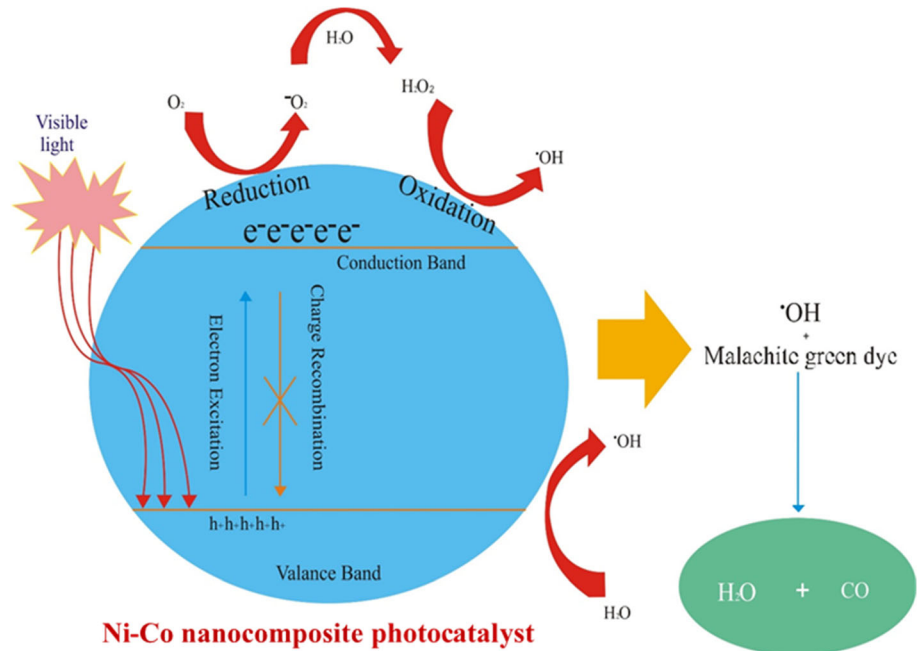
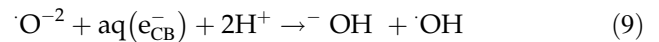
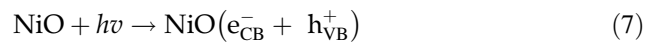
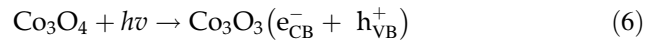


**Fig. 6** Recyclability of the  $\text{Co}_3\text{O}_4/\text{NiO}$  nanocomposite against MG dye

and 72% in the presence of  $\text{H}_2\text{O}_2$  and sugar, respectively, while EDTA brought about approximately 88% degradation of MG dye. The degradation process of MG with  $\text{Co}_3\text{O}_4/\text{NiO}$  probably be proceeded through the following photocatalytic reactions as shown in Eqs. 5–12, where the  $\text{h}^+$  and  $\cdot\text{O}_2^-$  radicals are involved in the photocatalysis of MG dye in the presence of  $\text{Co}_3\text{O}_4/\text{NiO}$  nanocomposite. Electrons in the conduction band (CB) of the catalyst are  $e^-_{\text{CB}}$ , while holes in the valence band (VB) are represented by  $\text{h}^+_{\text{VB}}$ . Thus, it is believed that  $\text{Co}_3\text{O}_4/\text{NiO}$

materials degraded the MG dye by generating  $\cdot\text{O}_2^-$  free radicals.



Under solar illumination,  $e^-$  and  $\text{h}^+$  are created in the CB and VB of both  $\text{Co}_3\text{O}_4$  and  $\text{NiO}$  photocatalysts (Eqs. 5 and 6) [50]. The photoexcited electrons are shifted to water, represented in Eq. 3, which acts as electron recipient and transport vehicle in photocatalysis, inhabiting the rejoining of photogenerated electron–hole pairs. The photocatalysis process takes place on the exterior of the  $\text{Co}_3\text{O}_4/\text{NiO}$  photocatalyst in a watery medium. The nano character of the further catalyst upsurges the surface area of the catalyst. The electrons are transferred from the catalyst and rejoin with surface-adsorbed oxygen to form  $\cdot\text{O}_2^-$  (Eq. 7) [51], which rejoins with  $\text{H}^+$  to make  $\cdot\text{OH}$  free radical (Eq. 8). Equally, the photochemical reduction

and photochemical oxidation beget hydroxyl free radical ( $\cdot\text{OH}$ ), which is accountable for the down gradation of MG. Simultaneously, the  $\text{h}^+$  is a highly oxidizing species [52];  $\text{h}^+$  is in the VB of  $\text{Co}_3\text{O}_4$  and can photo oxidize MG molecules [53, 54]. To be precise, those extremely energetic species react in chorus with MG molecules, ensuing in an effective photocatalysis (Eq. 12). The schematic mechanism is provided in Scheme 2.

### 3.4 Recyclability of catalyst

The constancy and restoration of the catalyst were studied by consuming 30 mL of 0.05 mM MG dye, to which 50 mg of the catalyst was added. For each study, the catalyst was recovered and laundered with enough water. The recovered catalysts were reused without any treatment for the elimination of MG dye. This testing was repeated till seven consecutive successions, and each time the catalyst maintained the activity with more negligible loss of inactivity, as shown in Fig. 6

## 4 Conclusion

In the current study,  $\text{Co}_3\text{O}_4/\text{NiO}$  nanocomposite was synthesized as a catalyst through the sol-gel method and utilized to degrade MG dye. Different characterization techniques, such as FESEM, XPS, XRD, TGA, UV-Vis, and BET, were used to investigate the synthesized catalyst. Thermocatalysis from 278 K to 313 K, photolysis (solar light), and photocatalysis in solar light were carried out to degrade MG dye. Besides, the effects of pH, temperature, concentration scavenger, and catalyst amount were studied experimentally. The  $k_{\text{app}}$  values for MG degradation in photocatalysis were  $3.95 \times 10^{-2} \text{ min}^{-1}$ , which is higher than those of photolysis ( $3.95 \times 10^{-3}$ ) and thermocatalysis ( $1.73 \times 10^{-2}$ ). These results indicated that the  $\text{Co}_3\text{O}_4/\text{NiO}$  nanocomposite is superior to catalyst activity in solar light as compared to thermocatalysis and photolysis. The results also revealed that the  $\text{Co}_3\text{O}_4/\text{NiO}$  nanocomposite showed the best results in basic medium, low concentration, and high catalyst dosage. The MG degradation mechanism by  $\text{Co}_3\text{O}_4/\text{NiO}$  nanocomposite under solar light was illustrated via  $\cdot\text{OH}$  as free radicals. It can be concluded that the  $\text{Co}_3\text{O}_4/\text{NiO}$  nanocomposite can be used effectively to degrade other pollutants.

## Acknowledgements

The Deanship of Scientific Research (DSR) at King Abdulaziz University (KAU), Jeddah, Saudi Arabia, has funded this project under grant no. (KEP-MSc: 55-247-1443)

## Author contributions

WUR contributed toward conceptional, methodology; formal analysis; investigation; data Curation; writing—original draft. TNK contributed toward methodology; investigation; data Curation; writing—original draft. AS contributed toward validation, data Curation; writing—review & editing. KS contributed toward investigation, writing—original draft. ZS contributed toward investigation, writing—original draft. SH contributed toward validation, writing—original draft. EMB contributed toward investigation, writing—original draft. HMA contributed toward investigation—writing—original draft. TMF contributed toward validation, writing—original draft. KA contributed toward investigation, writing—original draft. SBK contributed toward investigation, funding, writing—original draft. SAK contributed toward conceptional, supervision; formal analysis; investigation; data Curation; resources; writing—review & editing.

## Data availability

All data generated or analyzed during this study are included in the study.

## Declarations

**Conflict of interest** The authors declare that they have no conflict of interest.

**Ethical approval** Not applicable.

**Consent to publish** Not applicable.

**Consent to participate** Not applicable.

**Supplementary Information:** The online version contains supplementary material available at <http://doi.org/10.1007/s10854-022-09428-7>.

## References

1. H. Zeghioud, A.A. Assadi, N. Khellaf, H. Djelaf, A. Amrane, S. Rtimi, Photocatalytic performance of  $\text{Cu}_x\text{O}/\text{TiO}_2$  deposited by HiPIMS on polyester under visible light LEDs: oxidants, ions effect, and reactive oxygen species investigation. *Materials* **12**(3), 412 (2019)
2. S.A. Khan, S.B. Khan, T. Kamal, M. Yasir, A.M. Asiri, Antibacterial nanocomposites based on chitosan/Co-MCM as a selective and efficient adsorbent for organic dyes. *Int. J. Biol. Macromol.* **91**, 744–751 (2016). <https://doi.org/10.1016/j.ijbiomac.2016.06.018>
3. H. Zeghioud, A.A. Assadi, N. Khellaf, H. Djelaf, A. Amrane, S. Rtimi, Reactive species monitoring and their contribution for removal of textile effluent with photocatalysis under UV and visible lights: dynamics and mechanism. *J. Photochem. Photobiol. A* **365**, 94–102 (2018)
4. S. Hussain, M. Kamran, S.A. Khan, K. Shaheen, Z. Shah, H. Suo, Q. Khan, A.B. Shah, W.U. Rehman, Y.O. Al-Ghamdi, Adsorption, kinetics and thermodynamics studies of methyl orange dye sequestration through chitosan composites films. *Int. J. Biol. Macromol.* **168**, 383–394 (2021). <https://doi.org/10.1016/j.ijbiomac.2020.12.054>
5. S.A. Khan, S.B. Khan, A.M. Asiri, Layered double hydroxide of Cd-Al/C for the mineralization and de-coloration of dyes in solar and visible light exposure. *Sci. Rep.* **6**(1), 1–15 (2016). <https://doi.org/10.1038/srep35107>
6. R.R. Schio, N.P.G. Salau, E.S. Mallmann, G.L. Dotto, Modeling of fixed-bed dye adsorption using response surface methodology and artificial neural network. *Chem. Eng. Commun.* **208**(8), 1081–1092 (2021). <https://doi.org/10.1080/00986445.2020.1746655>
7. Y. Zhou, J. Lu, Y. Zhou, Y. Liu, Recent advances for dyes removal using novel adsorbents: a review. *Environ. Pollut.* **252**, 352–365 (2019). <https://doi.org/10.1016/j.envpol.2019.05.072>
8. A.C. Sadiq, N.Y. Rahim, F.B.M. Suah, Adsorption and desorption of malachite green by using chitosan-deep eutectic solvents beads. *Int. J. Biol. Macromol.* **164**, 3965–3973 (2020). <https://doi.org/10.1016/j.ijbiomac.2020.09.029>
9. T. Sakthivel, X. Huang, Y. Wu, S. Rtimi, Recent progress in black phosphorus nanostructures as environmental photocatalysts. *Chem. Eng. J.* **379**, 122297 (2020). <https://doi.org/10.1016/j.cej.2019.122297>
10. O. Alara, N. Abdurahman, S.A. Mudalip, O. Olalere, Effect of drying methods on the free radicals scavenging activity of *Vernonia amygdalina* growing in Malaysia. *J. King Saud Univ. Sci.* **31**(4), 495–499 (2019). <https://doi.org/10.1016/j.jksus.2017.05.018>
11. K.B. Tan, M. Vakili, B.A. Horri, P.E. Poh, A.Z. Abdullah, B. Salamatinia, Adsorption of dyes by nanomaterials: recent developments and adsorption mechanisms. *Sep. Purif. Technol.* **150**, 229–242 (2015). <https://doi.org/10.1016/j.seppur.2015.07.009>
12. A.A. Azzaz, S. Jellali, H. Akrouf, A.A. Assadi, L. Bousselmi, Optimization of a cationic dye removal by a chemically modified agriculture byproduct using response surface methodology: biomasses characterization and adsorption properties. *Environ. Sci. Pollut. Res.* **24**(11), 9831–9846 (2017). <https://doi.org/10.1007/s11356-016-7698-6>
13. N.S. Gilani, S.E. Tilami, S.N. Azizi, One-step green synthesis of nano-sodalite zeolite and its performance for the adsorptive removal of crystal violet. *J. Chin. Chem. Soc.* **68**, 2264 (2021). <https://doi.org/10.1002/jccs.202100258>
14. S. Garcia-Segura, M.M.S.G. Eiband, J.V. de Melo, C.A. Martínez-Huitle, Electrocoagulation and advanced electrocoagulation processes: a general review about the fundamentals, emerging applications and its association with other technologies. *J. Electroanal. Chem.* **801**, 267–299 (2017). <https://doi.org/10.1016/j.jelechem.2017.07.047>
15. S. Garcia-Segura, L.M. Bellotindos, Y.-H. Huang, E. Brillas, M.-C. Lu, Fluidized-bed Fenton process as alternative wastewater treatment technology: a review. *J. Taiwan Inst. Chem. Eng.* **67**, 211–225 (2016). <https://doi.org/10.1016/j.jtice.2016.07.021>
16. K. Almashhori, T.T. Ali, A. Saeed, R. Alwafi, M. Aly, F.E. Al-Hazmi, Antibacterial and photocatalytic activities of controllable (anatase/rutile) mixed phase  $\text{TiO}_2$  nanophotocatalysts synthesized via a microwave-assisted sol–gel method. *New J. Chem.* **44**(2), 562–570 (2020). <https://doi.org/10.1039/C9NJ03258D>
17. S. Garcia-Segura, E. Brillas, Applied photoelectrocatalysis on the degradation of organic pollutants in wastewaters. *J. Photochem. Photobiol. C* **31**, 1–35 (2017). <https://doi.org/10.1016/j.jphotochemrev.2017.01.005>
18. M. Gonçalves, M.C. Guerreiro, P.H. Ramos, L.C.A. de Oliveira, K. Sapag, Activated carbon prepared from coffee pulp: potential adsorbent of organic contaminants in aqueous solution. *Water Sci. Technol.* **68**(5), 1085–1090 (2013). <https://doi.org/10.2166/wst.2013.349>
19. A.A. Azzaz, A.A. Assadi, S. Jellali, A. Bouzaza, D. Wolbert, S. Rtimi, L. Bousselmi, Discoloration of simulated textile effluent in continuous photoreactor using immobilized titanium dioxide: effect of zinc and sodium chloride. *J. Photochem. Photobiol. A* **358**, 111–120 (2018)
20. H. Meriem, D. Souad, T. Lakhdar, Synthesis of copper with sodium ascorbate and its application in malachite green discoloration. *J. Environ. Chem. Eng.* **8**(5), 104457 (2020). <https://doi.org/10.1016/j.jece.2020.104457>

21. N.P. Raval, P.U. Shah, N.K. Shah, Malachite green “a cationic dye” and its removal from aqueous solution by adsorption. *Appl. Water Sci.* **7**(7), 3407–3445 (2017). <https://doi.org/10.1007/s13201-016-0512-2>
22. C. Chen, C. Lu, Y. Chung, J. Jan, UV light induced photodegradation of malachite green on TiO<sub>2</sub> nanoparticles. *J. Hazard. Mater.* **141**(3), 520–528 (2007)
23. A. Mohamed, W. Nasser, T. Osman, M. Toprak, M. Muhammed, A. Uheida, Removal of chromium (VI) from aqueous solutions using surface modified composite nanofibers. *J. Colloid Interface Sci.* **505**, 682–691 (2017). <https://doi.org/10.1016/j.jcis.2017.06.066>
24. S. Saha, J. Wang, A. Pal, Nano silver impregnation on commercial TiO<sub>2</sub> and a comparative photocatalytic account to degrade malachite green. *Sep. Purif. Technol.* **89**, 147–159 (2012). <https://doi.org/10.1016/j.seppur.2012.01.012>
25. P. Raizada, P. Singh, A. Kumar, B. Pare, S.B. Jonnalagadda, Zero valent iron-brick grain nanocomposite for enhanced solar-Fenton removal of malachite green. *Sep. Purif. Technol.* **133**, 429–437 (2014). <https://doi.org/10.1016/j.seppur.2014.07.012>
26. C. Byrne, S. Dervin, D. Hermosilla, N. Merayo, Á. Blanco, S. Hinder, M. Harb, D.D. Dionysiou, S.C. Pillai, Solar light assisted photocatalytic degradation of 1,4-dioxane using high temperature stable anatase W-TiO<sub>2</sub> nanocomposites. *Catal. Today* **380**, 199–208 (2021). <https://doi.org/10.1016/j.cattod.2021.02.001>
27. P. Ganguly, S. Mathew, L. Clarizia, S. Kumar, A. Akande, S.J. Hinder, A. Breen, S.C. Pillai, Ternary metal chalcogenide heterostructure (AgInS<sub>2</sub>-TiO<sub>2</sub>) nanocomposites for visible light photocatalytic applications. *ACS Omega* **5**(1), 406–421 (2020). <https://doi.org/10.1021/acsomega.9b02907>
28. P. Suyana, P. Ganguly, B.N. Nair, S.C. Pillai, U.S. Hareesh, Structural and compositional tuning in g-C<sub>3</sub>N<sub>4</sub> based systems for photocatalytic antibiotic degradation. *Chem. Eng. J. Adv.* **8**, 100148 (2021). <https://doi.org/10.1016/j.cej.2021.100148>
29. R. Kottappara, S. Palantavida, S.C. Pillai, B.K. Vijayan, Composition tuning in copper - oxide decorated reduced graphene oxide yields efficient photo- and reduction catalysts. *Surf. Interfaces* **22**, 100792 (2021). <https://doi.org/10.1016/j.surfin.2020.100792>
30. S. Rtimi, C. Pulgarin, R. Sanjines, J. Kiwi, Innovative semi-transparent nanocomposite films presenting photo-switchable behavior and leading to a reduction of the risk of infection under sunlight. *RSC Adv.* **3**(37), 16345–16348 (2013). <https://doi.org/10.1039/C3RA42762E>
31. M.A. Gabal, A.A. Al-Juaid, S. El-Rashed, M.A. Hussein, Y.M. Al-Angari, A. Saeed, Structural, thermal, magnetic and electrical properties of polyaniline/CoFe<sub>2</sub>O<sub>4</sub> nano-composites with special reference to the dye removal capability. *J. Inorg. Organomet. Polym. Mater.* **29**(6), 2197–2213 (2019). <https://doi.org/10.1007/s10904-019-01179-z>
32. S.A. Khan, S.B. Khan, A.M. Asiri, Core-shell cobalt oxide mesoporous silica based efficient electro-catalyst for oxygen evolution. *New J. Chem.* **39**(7), 5561–5569 (2015). <https://doi.org/10.1039/C5NJ00521C>
33. S.A. Khan, S.B. Khan, A.M. Asiri, Toward the design of Zn–Al and Zn–Cr LDH wrapped in activated carbon for the solar assisted de-coloration of organic dyes. *RSC Adv.* **6**(86), 83196–83208 (2016). <https://doi.org/10.1039/C6RA10598J>
34. S.B. Khan, S.A. Khan, A.M. Asiri, A fascinating combination of Co, Ni and Al nanomaterial for oxygen evolution reaction. *Appl. Surf. Sci.* **370**, 445–451 (2016). <https://doi.org/10.1016/j.apsusc.2016.02.062>
35. M. Cheng, H. Fan, Y. Song, Y. Cui, R. Wang, Interconnected hierarchical NiCo<sub>2</sub>O<sub>4</sub> microspheres as high-performance electrode materials for supercapacitors. *Dalton Trans.* **46**(28), 9201–9209 (2017). <https://doi.org/10.1039/C7DT01289F>
36. S.R. Alharbi, M. Alhassan, O. Jalled, S. Wageh, A. Saeed, Structural characterizations and electrical conduction mechanism of CaBi<sub>2</sub>Nb<sub>2</sub>O<sub>9</sub> single-phase nanocrystallites synthesized via sucrose-assisted sol-gel combustion method. *J. Mater. Sci.* **53**(16), 11584–11594 (2018). <https://doi.org/10.1007/s10853-018-2458-2>
37. S.S.J. Aravind, V. Eswaraiyah, S. Ramaprabhu, Facile and simultaneous production of metal/metal oxide dispersed graphene nano composites by solar exfoliation. *J. Mater. Chem.* **21**(43), 17094–17097 (2011). <https://doi.org/10.1039/C1JM13626G>
38. Z.N. Kayani, M.Z. Butt, S. Riaz, S. Naseem, Synthesis of NiO nanoparticles by sol-gel technique. *Mater. Sci.* **36**(4), 547–552 (2019). <https://doi.org/10.2478/msp-2018-0088>
39. R. Ramasamy, K. Ramachandran, G.G. Philip, R. Ramachandran, H.A. Therese, G. Gnana Kumar, Design and development of Co<sub>3</sub>O<sub>4</sub>/NiO composite nanofibers for the application of highly sensitive and selective non-enzymatic glucose sensors. *RSC Adv.* **5**(93), 76538–76547 (2015). <https://doi.org/10.1039/C5RA11739A>
40. M.N. Siddique, A. Ahmed, T. Ali, P. Tripathi, Investigation of optical properties of nickel oxide nanostructures using photoluminescence and diffuse reflectance spectroscopy. *AIP Conf. Proc.* **1953**(1), 030027 (2018). <https://doi.org/10.1063/1.5032362>
41. R. Malik, V.K. Tomer, Y.K. Mishra, L. Lin, Functional gas sensing nanomaterials: a panoramic view. *Appl. Phys. Rev.* **7**(2), 021301 (2020). <https://doi.org/10.1063/1.5123479>
42. X. Song, L. Gao, S. Mathur, Synthesis, characterization, and gas sensing properties of porous nickel oxide nanotubes. *J. Phys. Chem. C* **115**(44), 21730–21735 (2011). <https://doi.org/10.1021/jp208093s>

43. X. Sun, X. Hu, Y. Wang, R. Xiong, X. Li, J. Liu, H. Ji, X. Li, S. Cai, C. Zheng, Enhanced gas-sensing performance of Fe-doped ordered mesoporous NiO with long-range periodicity. *J. Phys. Chem. C* **119**(6), 3228–3237 (2015). <https://doi.org/10.1021/jp5124585>
44. E.U. Ikuhoria, S.O. Omorogbe, B.T. Sone, M. Maaza, Bioinspired shape controlled antiferromagnetic Co<sub>3</sub>O<sub>4</sub> with prism like-anchored octahedron morphology: a facile green synthesis using Manihot esculenta Crantz extract. *Sci. Technol. Mater.* **30**(2), 92–98 (2018). <https://doi.org/10.1016/j.stmat.2018.02.003>
45. C.T. Anuradha, P. Raji, Facile synthesis and characterization of Co<sub>3</sub>O<sub>4</sub> nanoparticles for high-performance supercapacitors using *Camellia sinensis*. *Appl. Phys. A* **126**(3), 164 (2020). <https://doi.org/10.1007/s00339-020-3352-8>
46. A. Vennela, D. Mangalaraj, N. Muthukumarasamy, S. Agilan, K.J. Hemalatha, Structural and optical properties of Co<sub>3</sub>O<sub>4</sub> nanoparticles prepared by sol-gel technique for photocatalytic application. *Int. J. Electrochem. Sci.* **14**(4), 3535–3552 (2019). <https://doi.org/10.20964/2019.04.40>
47. M. Pooresmaeil, H. Namazi, Chapter 14 - Application of polysaccharide-based hydrogels for water treatments, in *Hydrogels Based on Natural Polymers*. ed. by Y. Chen (Elsevier, Amsterdam, 2020), pp.411–455
48. Y. Zhu, J. Xue, T. Xu, G. He, H. Chen, Enhanced photocatalytic activity of magnetic core-shell Fe<sub>3</sub>O<sub>4</sub>@ Bi<sub>2</sub>O<sub>3</sub>-RGO heterojunctions for quinolone antibiotics degradation under visible light. *J. Mater. Sci.-Mater. Electron.* **28**(12), 8519–8528 (2017). <https://doi.org/10.1007/s10854-017-6574-6>
49. L. Ye, J. Liu, C. Gong, L. Tian, T. Peng, L. Zan, Two different roles of metallic Ag on Ag/AgX/BiOX (X= Cl, Br) visible light photocatalysts: surface plasmon resonance and Z-scheme bridge. *ACS Catal.* **2**(8), 1677–1683 (2012). <https://doi.org/10.1021/cs300213m>
50. Y. Ao, L. Xu, P. Wang, C. Wang, J. Hou, J. Qian, Y. Li, Graphene and TiO<sub>2</sub> co-modified flower-like Bi<sub>2</sub>O<sub>3</sub>CO<sub>3</sub>: a novel multi-heterojunction photocatalyst with enhanced photocatalytic activity. *Appl. Surf. Sci.* **355**, 411–418 (2015). <https://doi.org/10.1016/j.apsusc.2015.07.027>
51. H. Liu, W.-R. Cao, Y. Su, Z. Chen, Y. Wang, Bismuth oxyiodide-graphene nanocomposites with high visible light photocatalytic activity. *J. Colloid Interface Sci.* **398**, 161–167 (2013). <https://doi.org/10.1016/j.jcis.2013.02.007>
52. R. Montenegro-Ayo, J.C. Morales-Gomero, H. Alarcon, S. Cotillas, P. Westerhoff, S. Garcia-Segura, Scaling up photo-electrocatalytic reactors: a TiO<sub>2</sub> nanotube-coated disc compound reactor effectively degrades acetaminophen. *Water* **11**(12), 2522 (2019). <https://doi.org/10.3390/w11122522>
53. X. Zhang, R. Li, M. Jia, S. Wang, Y. Huang, C. Chen, Degradation of ciprofloxacin in aqueous bismuth oxybromide (BiOBr) suspensions under visible light irradiation: a direct hole oxidation pathway. *Chem. Eng. J.* **274**, 290–297 (2015). <https://doi.org/10.1016/j.cej.2015.03.077>
54. P. Huo, Y. Tang, M. Zhou, J. Li, Z. Ye, C. Ma, L. Yu, Y. Yan, Fabrication of ZnWO<sub>4</sub>-CdS heterostructure photocatalysts for visible light induced degradation of ciprofloxacin antibiotics. *J. Ind. Eng. Chem.* **37**, 340–346 (2016). <https://doi.org/10.1016/j.jiec.2016.03.043>

**Publisher's Note** Springer Nature remains neutral with regard to jurisdictional claims in published maps and institutional affiliations.

Springer Nature or its licensor (e.g. a society or other partner) holds exclusive rights to this article under a publishing agreement with the author(s) or other rightsholder(s); author self-archiving of the accepted manuscript version of this article is solely governed by the terms of such publishing agreement and applicable law.